Journal of Alloys and Compounds 505 (2010) 404–415

Contents lists available at ScienceDirect

Journal of Alloys and Compounds

journal homepage: www.elsevier.com/locate/jallcom

Magnetic structures of orthorhombic rare earth stannides LSn_2 (L = Tb–Tm)

G. Venturini[a,*], P. Lemoine[a], B. Malaman[a], B. Ouladdiaf[b]

[a] Institut Jean Lamour, CNRS (UMR 7198) - Nancy Université, B.P. 70239, 54506 Vandoeuvre-les-Nancy Cedex, France
[b] Institut Laue-Langevin, Boite Postale 156, 38042 Grenoble Cedex 9, France

ARTICLE INFO

Article history:
Received 8 February 2010
Received in revised form 14 June 2010
Accepted 15 June 2010
Available online 25 June 2010

Keywords:
Rare-earth alloys and compounds
Neutron diffraction

ABSTRACT

The magnetic structures of the orthorhombic compounds LSn_2 (S.G.: Cmcm; L = Tb–Tm) have been determined from neutron diffraction studies. The compounds LSn_2 (L = Tb, Dy, Ho Er) order below 26.7, 17.2, 7.8 and 4.5 K, respectively, in a sine-modulated structure characterized by the propagation vector $k = (\approx 0.39, 0, \approx 0.41)$. Below 12.7, 5, 4.8 and 2 K, respectively, these compounds undergo a transition towards a collinear antiferromagnetic structure characterized by the propagation vector $k = (0, 0, 1/2)$ for Tb and Er, $k = (1/2, 1/2, 0)$ for Ho and $k = (1/2, 1/2, 1/2)$ for Dy. The compound $TmSn_2$ orders below 4.0 K in a sine-modulated structure characterized by the propagation vector $k = (0, 0.667, 0.380)$. The moment direction is close to [0 0 1] for L = Tb, Dy, Ho and aligned along [1 0 0] for L = Er, Tm. The results are discussed and a relative scale of the stability of the moment configuration in the (0 1 0) plane is proposed.

1. Introduction

The LT_xSn_2 compounds crystallize in the defective $CeNiSi_2$-type structure [1]. The magnetic properties of the L = Tb–Er; T = Co, Ni derivatives have been studied by magnetisation measurements and powder neutron diffraction experiments [2–5]. The terbium and erbium compounds are antiferromagnetic and their magnetic structures are characterized by the same propagation vector $k = (0, 0, 1/2)$. The holmium compounds are also antiferromagnetic but their magnetic structures are characterized by another propagation vector $k = (1/2, 1/2, 0)$. Contrary to the others, the compound $DyNi_{0.22}Sn_2$ displays a sine-modulated structure with propagation vector $k = (0.361, 0, 0.343)$.

The compounds $DyFe_xSn_2$ ($0.0 < x < 0.3$) have been studied by magnetisation measurements and Mössbauer spectroscopy [6] and an exhaustive neutron diffraction study of the LFe_xSn_2 series (L = Tb–Tm) has been reported very recently [7]. It has been observed that the terbium, holmium and erbium compounds behave like the corresponding cobalt and nickel representatives and, this time, $DyFe_{0.15}Sn_2$ exhibits a magnetic structure similar to that of $TbFe_{0.15}Sn_2$. The sine-modulated magnetic structure observed for $TmFe_{0.1}Sn_2$ is of a new kind, characterized by the propagation vector $k = (0, 0.7196, 0.4381)$.

These bibliographic items show that, except for the dysprosium compounds, the behaviour of the studied compounds does not greatly vary with the nature of the transition metal, a feature which might be related to the relatively low contents in these elements. In order to check this assumption, it has been decided to perform a neutron diffraction study of the corresponding $ZrSi_2$-type LSn_2 compounds ("empty $CeNiSi_2$-phases") which magnetic structures have, up to now, never been determined.

2. Experimental methods

The samples have been prepared in an induction furnace starting from the elements in stoichiometric amounts. According to the thermal stability range of the compounds LSn_2 [8], the resulting ingots are annealed at 1123 K during two weeks. The samples have been checked by conventional X-ray powder analysis (XPERT Pro Cu Kα). The magnetisation measurements have been performed on a MANICS magneto-susceptometer in the temperature range 4.2–300 K and in fields up to 1.5 T. The neutron diffraction patterns have been recorded on the D1B diffractometer at the Institut Laue Langevin (Grenoble) using the wavelength (λ = 2.520 Å). In the case of $DySn_2$, in order to minimize neutron absorption, a special double-wall vanadium sample holder was used. Long duration patterns have been recorded in the different magnetic states. In the case of $TbSn_2$ and $HoSn_2$, thermograms have been recorded to check the thermal variation of the intensity of the magnetic lines. The structures have been refined using the Fullprof software [9].

3. Crystallographic data

The $ZrSi_2$-type compounds [10] crystallize in the orthorhombic symmetry with the space group Cmcm (Fig. 1). All atoms occupy a 4(c) position, namely $(0, y, 1/4)$. The cell parameters, refined at room temperature from X-ray diffraction data, are given in Table 1. They are in fair accordance with the results of previous studies [11–13].

Regarding the coordination shell of the L atoms, the structure may be considered as a stacking of Sn_8 Archimedean antiprisms centred by the L atom (Fig. 1). Regarding the L sublattice, the structure may be also viewed as infinite sheets of L_6 trigonal prisms sharing their faces. These sheets, perpendicular to the [0 1 0] direction, are linked together building L_4 tetrahedrons stretched along

* Corresponding author. Tel.: +33 3 83 68 46 73; fax: +33 3 83 68 46 11.
E-mail address: Gerard.Venturini@lcsm.uhp-nancy.f (G. Venturini).

0925-8388/$ – see front matter © 2010 Elsevier B.V. All rights reserved.
doi:10.1016/j.jallcom.2010.06.089

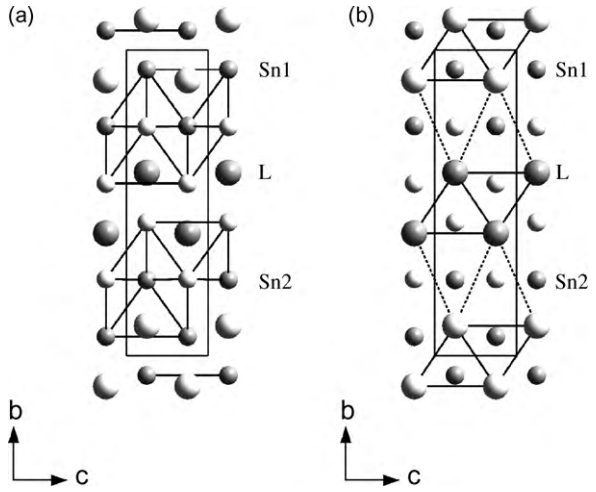

Fig. 1. Crystal structure of $ZrSi_2$-type LSn_2 compounds: (a) stacking of the Sn_8 Archimedian antiprisms and (b) stacking of the L_6 trigonal prisms (full lines) and L_4 stretched tetrahedra (dotted lines).

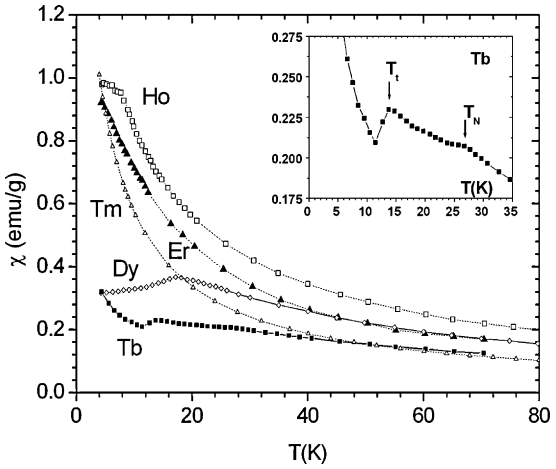

Fig. 2. Thermal variation of the susceptibility of LSn_2 compounds (L = Tb–Tm) under an applied field of 0.5 T (insert shows the two transition in $TbSn_2$).

Table 1
Cell parameters measured at room temperature and thermomagnetic results of LSn_2 compounds.

	a (Å)	b (Å)	c (Å)	V (Å^3)	T_N	T_t
$TbSn_2$	4.4040(2)	16.2900(6)	4.3076(2)	309.03(3)	26.7	12.7
$DySn_2$	4.3895(32)	16.230(1)	4.2990(3)	306.27(4)	17.2	–
$HoSn_2$	4.3762(2)	16.1790(6)	4.2905(2)	303.78(2)	7.8	6.2/4.8
$ErSn_2$	4.3662(3)	16.1288(8)	4.2856(3)	301.80(3)	4.5	–
$TmSn_2$	4.3560(3)	16.0615(7)	4.2766(3)	299.21(3)	–	–

[0 1 0]. According to Refs. [2–5], the four L moments in each chemical cell will be numbered as follows: μ_1 (0, y, 1/4), μ_2 (0, $-y$, 3/4), μ_3 (1/2, $y+(1/2)$, 1/4), μ_4 (1/2, $(1/2)-y$, 3/4).

4. Magnetisation measurements

The magnetisation measurements performed at 4.2 K in fields up to 1.5 T are characterized by the absence of spontaneous magnetisation and by a linear variation. The thermomagnetic curve of the compound $TbSn_2$ is characterized by a Néel point at 26.7 K and a second magnetic transition around 13 K (Fig. 2 and Table 2). The compounds $DySn_2$ and $ErSn_2$ display only one Néel point at T_N = 17.2 and 4.5 K, respectively. For $DySn_2$, we do not observe the second transition previously observed at 5 K by ac susceptibility measurements [6]. The curve of the compound $HoSn_2$ displays a

Table 2
Refined parameters of $TbSn_2$ at 45, 17 and 1.9 K.

T	45 K	17 K	1.9 K
a (Å)	4.388(1)	4.387(1)	4.388(1)
b (Å)	16.241(5)	16.230(4)	16.230(3)
c (Å)	4.288(2)	4.281(1)	4.284(1)
y_{Tb}	0.1010(7)	0.0992(4)	0.1034(8)
y_{Sn_1}	0.4394(8)	0.438(1)	0.436(1)
y_{Sn_2}	0.7464(6)	0.7444(9)	0.748(1)
f_{corr}	0.08(1)	0.10(1)	0.11(1)
A_{Tb}(I) (μ_B)	0	8.81(6)	0
θ_{Tb} (°)	–	17(1)	–
ϕ_{Tb} (°)	–	90	–
α_{Tb} (°)	–	239(2)	–
q_x	–	0.3916(2)	–
q_y	–	0	–
q_z	–	0.4159(1)	–
μ_{Tb}(II) (μ_B)	0	0	8.8(2)
θ_{Tb} (°)	–	–	12.8(2)
ϕ_{Tb} (°)	–	–	90
q_x	–	–	0
q_y	–	–	0
q_z	–	–	1/2
r_{Bragg}; r_f	2.40; 5.33	1.98; 2.26	2.57; 4.20
$r_{magnI,II}$	–; –	4.89; –	–; 4.41
R_{wp}; R_{exp}	7.17; 2.58	8.62; 1.80	8.44; 1.00
χ^2	9.05	23.0	71.2

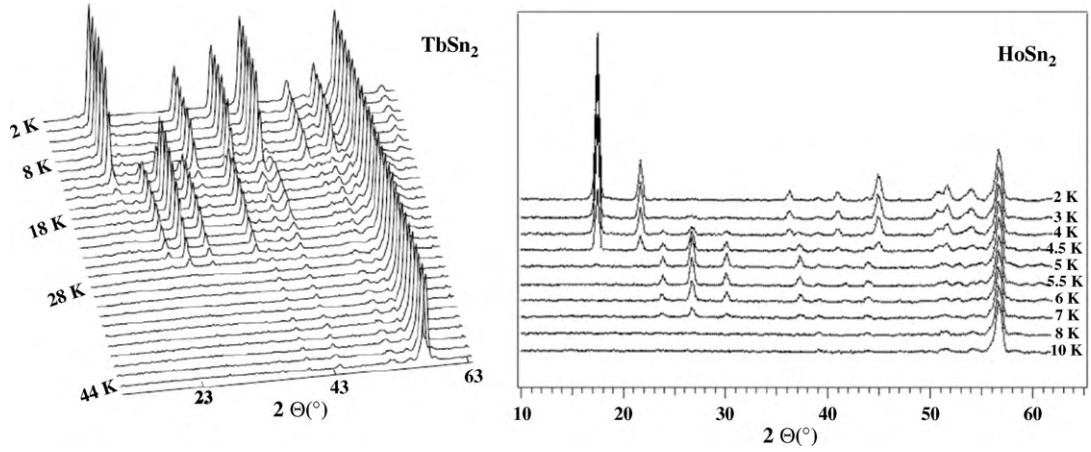

Fig. 3. Neutron thermograms of $TbSn_2$ and $HoSn_2$.

Néel point at 7.8 K and slight anomalies around 6.2 and 4.8 K while we do not observed any magnetic transition for the compound $TmSn_2$, at least above 4.2 K.

5. Neutron diffraction results

In all cases, the neutron diffraction patterns recorded above T_N only show the nuclear reflections corresponding to the $ZrSi_2$ type-structure, the main lines of elemental tin and, sometimes, very weak lines of impurities which will be discussed in the corresponding sections.

Below T_N, each sample exhibits a second transition at various T_t, in agreement with the magnetic measurements. As an example, the neutron thermograms of $TbSn_2$ and $HoSn_2$ are displayed in Fig. 3.

Between T_N and T_t, the neutron diffraction patterns of Tb-, Dy-, Ho- and $ErSn_2$ are similar to that observed for $DyNi_{0.22}Sn_2$ and characterized by a propagation vector $k = (q_x, 0, q_z)$ (see Section 2 of Ref. [4]) yielding the same incommensurate magnetic behaviour of the L sublattice. According to the observed satellites $(h\,k\,l)^{+\text{or}-}$ with $h + k = 2n$, the refinements have been done considering a C-centred sine-modulated structure and refining the components q_x and q_z of the propagation vector, the maximum moment amplitude A_L, the phase angle α between the L atoms related by the *c*-glide plane and the Euler angles θ and ϕ (relative to the *c*-parameter of the orthorhombic cell). It is noteworthy that, below T_t, each compound behaves singularly (Fig. 3) and a careful analysis of the patterns recorded at 2 K is now necessary to clarify this point.

Finally, it is worth noting that the $TmSn_2$ compound exhibits original patterns in its whole ordered range. This point will be described in Section 5.5.

5.1. Magnetic structures of $TbSn_2$

The neutron diffraction pattern recorded in the paramagnetic state (Fig. 4) exhibits some extra lines which can be indexed considering a Dy_5Sn_{11}-type Tb_5Sn_{11} impurity [14]. Although these lines are very weak, the refinement yields a significant improvement of the χ^2 value from 18.1 to 9.05. This effect arises from the fact that both $ZrSi_2$ and Dy_5Sn_{11}-types are closely related (*FCC derivatives*) and that the four main lines of the $TbSn_2$ phase are convoluted with the four main lines of the Tb_5Sn_{11} phase.

Below $T_N \approx 27$ K, one observes a growth of magnetic lines in good accordance with the Néel temperature determined by magnetisation measurements. Below $T_t \approx 14$ K, these magnetic lines begin to vanish and some other magnetic lines grow (Fig. 3). This observation is in fair agreement with the second magnetic transition detected at 12.7 K by magnetic measurements.

The neutron diffraction pattern recorded at 17 K is shown in Fig. 4. The refinements clearly confirm the incommensurate magnetic structure previously observed for $DyNi_{0.22}Sn_2$ with a propagation vector $k = (0.3916(2), 0, 0.4159(1))$. The results are given in Table 2 and the magnetic structure is depicted in Fig. 5a and b. The weak remaining lines observed around $2\theta = 20°$ have been fairly well indexed considering the magnetic structure of Tb_5Sn_{11} [15]. The local arrangement of the moments (corresponding to the shortest distances in the Tb–Tb pairs) is depicted in Fig. 5c and the observed phase differences between the moments are summarized in Table 3.

The low temperature pattern is fairly well indexed considering the antiferromagnetic structure AF1 observed for $TbFe_xSn_2$ [7]. The refinements have been therefore undertaken considering the moment arrangement $\mathbf{A} = \mu_1 - \mu_2 - \mu_3 + \mu_4$, previously defined for the AF1 structure [7] and refining the Tb moment value μ_{Tb} and the Euler angles θ_{Tb} and ϕ_{Tb}. This leads to a rather good reliability factor ($r_{magn} = 4.51\%$) but there are subsequent "S-shaped" misfits related

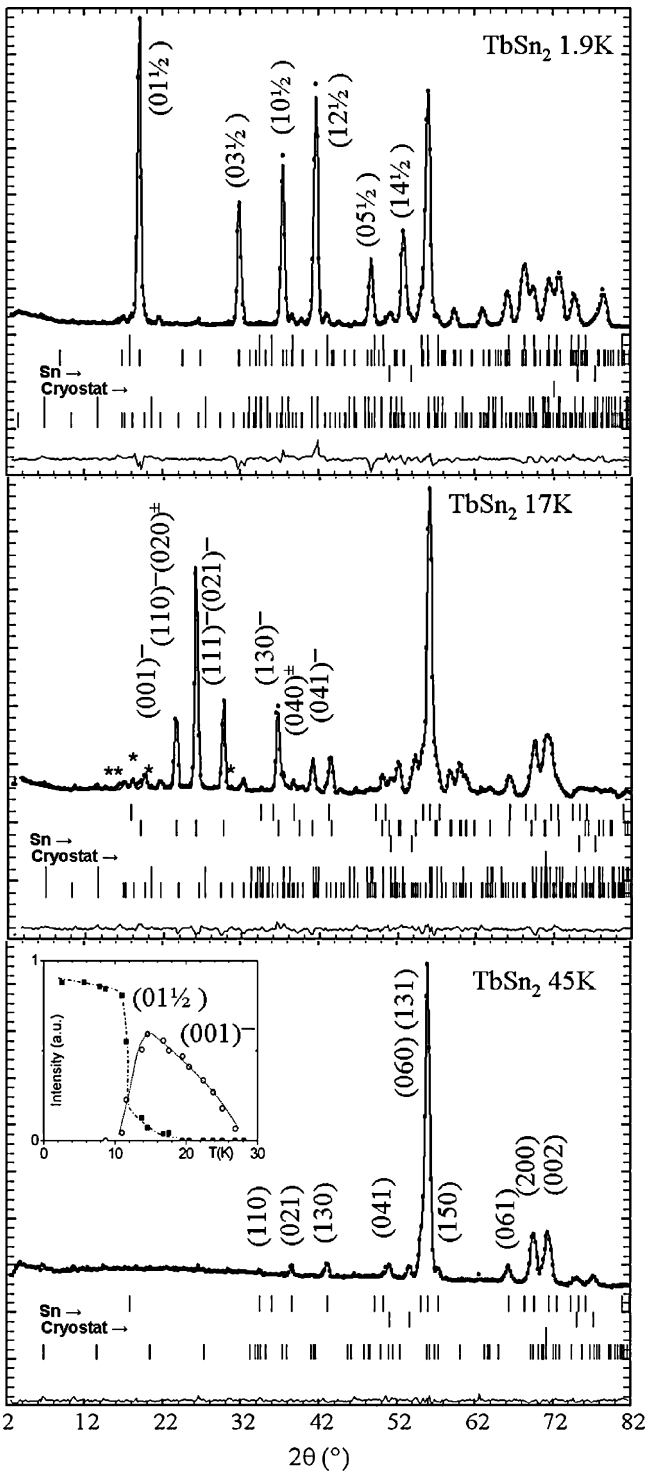

Fig. 4. Observed and calculated neutron diffraction patterns of $TbSn_2$ at 45, 17 and 1.9 K (insert shows the variation of several typical lines and * indicate the magnetic lines of the Tb_5Sn_{11} impurity).

to the two first magnetic lines. Owing to the facts that (i) this misfit lies in the high Bragg angle part of the (0, 1, 1/2) line and in the low Bragg angle part of the (0, 3, 1/2) line (ii) the intensity of the (0, 1, 1/2) line is calculated stronger than that of the (0, −1, 1/2) line (iii) the intensity of the (0, 3, 1/2) line is calculated weaker than that of the (0, −3, 1/2) line (Fig. 4c), it is suggested that it may arise from a monoclinic deformation of the cell. Attempts to refine the α angle between the **b** and **c** parameters in a monoclinic system lead to

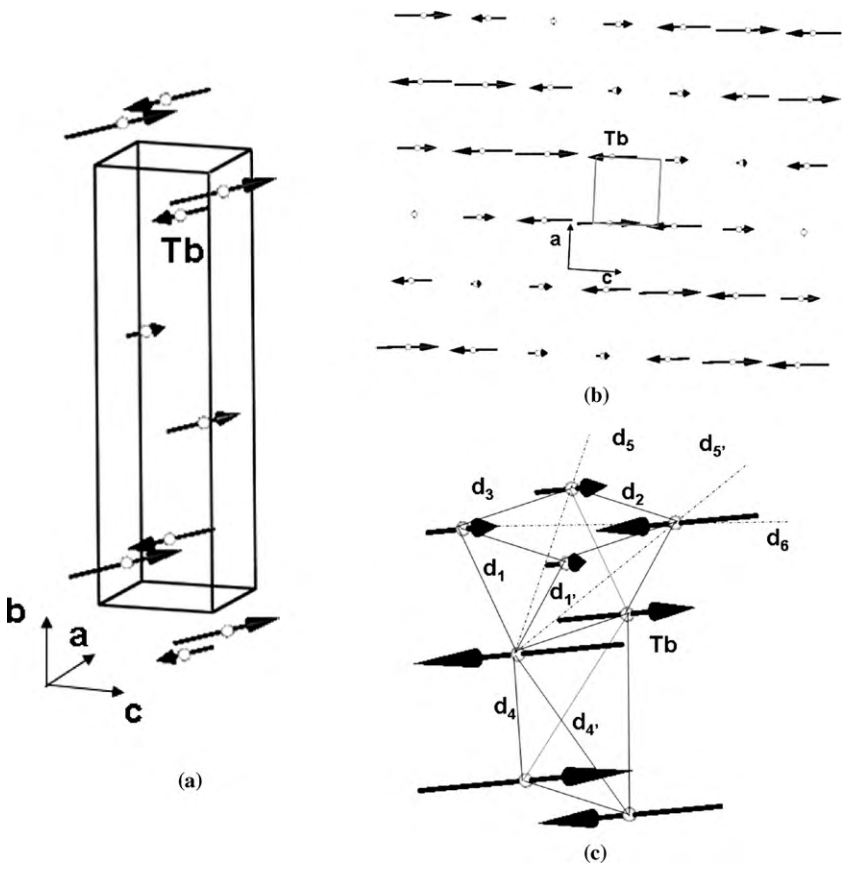

Fig. 5. Sine-modulated magnetic structure of $TbSn_2$ (a), arrangement of the moments in the (0 1 0) plane (b) and local arrangement of the Tb moments in the trigonal prism and stretched tetrahedron (c).

the value $\alpha = 89.81(2)^\circ$ and improve the χ^2 value from 105 to 71.2 without significant changes of the reliability factor ($r_{magn} = 4.41\%$). The results of the refinement are gathered in Table 2. At 1.9 K, the Tb moment is close to the theoretical free ion value.

The magnetic structure is depicted in Fig. 6. The moments are arranged in ferromagnetic slabs parallel to the $(0\,1\,1)_m$ plane and these slabs are antiferromagnetically coupled with the adjacent ones along the stacking direction. The local arrangement of the moments (*corresponding to the shortest distances in the Tb–Tb pairs*) is depicted in Fig. 6b and the observed phase differences between the moments are summarized in Table 3. This local arrangement is characterized by many frustrated situations: d_1 and $d_{1'}$ in the trigonal face of the prism, d_5 and $d_{5'}$ in the shortest diagonal of the prism, d_4 and $d_{4'}$ in the stretched tetrahedron. There are only

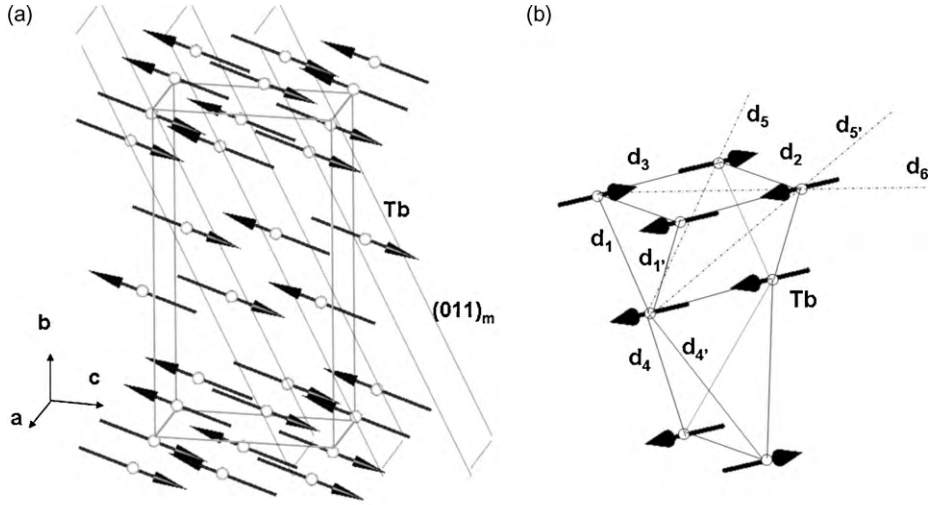

Fig. 6. Antiferromagnetic structure of $TbSn_2$ (a) and local arrangement of the Tb moments in the trigonal prism and stretched tetrahedron (b).

Table 3
Observed phase differences (°) between the moments of the L atoms belonging to the trigonal prism and stretched tetrahedron in the commensurate and incommensurate structure (see Figs. 4, 5, 7, 9 and 12).

L pairs through	d_{Ho-Ho} (Å)	Tb_{com}	Tb_{inc}	Dy_{com}	Ho_{com}	Tm_{inc}
d_1	3.817	0	46	180	0	116
$d_{1'}$	3.817	180	164	0	0	107
d_2	4.284	180	150	180	0	137
d_3	4.373	0	141	180	180	0
d_4	5.785	0	117	0	0	123
$d_{4'}$	5.785	180	94	180	180	13
d_5	5.804	0	173	0	180	116
$d_{5'}$	5.804	180	23	180	180	107
d_6	6.122	180	69	0	180	137

three non-frustrated pairs: d_3 (parallel arrangement along [1 0 0]), d_2 (antiparallel arrangement along [0 0 1]) and d_6 (diagonal of the pseudo-square).

Remark: The monoclinic deformation, suggested by the improvement of the χ^2 factor, might be related to a partial remote of the frustrated situations. Assuming no variation of the atomic positions and considering the structure description in ferromagnetic (0 1 1) planes antiferromagnetically coupled, the effect of the observed monoclinic distortion ($\alpha < 90°$) will be to shorten the distance $d_{1'}$ corresponding to the parallel arrangement and to enlarge the equivalent distance d_1 corresponding to the antiparallel arrangement.

It is worth noting that, in both high and low temperature magnetic structures, the moment direction lies in the (1 0 0) plane and is close to the [0 0 1] direction.

5.2. Magnetic structures of $DySn_2$

The pattern recorded at 9 K (Fig. 7) is similar to that previously observed for $TbSn_2$ at 17 K yielding a quite similar propagation vector (0.3921(5), 0, 0.4150(4)) and the same conclusions.

Below 5 K, one observes the growth of additional magnetic lines at $2\theta \approx 28$, 33 an 48° (Fig. 7), in fair agreement with the ac susceptibility measurements of Ref. [5]. Attempts to index them led us to consider the magnetic cell ($a_m = 2a_c$; $b_m = 2b_c$; $c_m = 2c_c$). The eight possible moment arrangements in the chemical cell, namely:

$+\mu_1$	$-\mu_1$	$+\mu_1$	$+\mu_1$	$+\mu_1$	$+\mu_1$	$+\mu_1$	$+\mu_1$
$+\mu_2$	$+\mu_2$	$-\mu_2$	$+\mu_2$	$+\mu_2$	$-\mu_2$	$-\mu_2$	$+\mu_2$
$+\mu_3$	$+\mu_3$	$+\mu_3$	$-\mu_3$	$+\mu_3$	$-\mu_3$	$+\mu_3$	$-\mu_3$
$+\mu_4$	$+\mu_4$	$+\mu_4$	$+\mu_4$	$-\mu_4$	$+\mu_4$	$-\mu_4$	$-\mu_4$

have been tested. We observed that only the arrangements ($-\mu_1 = +\mu_2 = +\mu_3 = +\mu_4$) and ($+\mu_1 = -\mu_2 = +\mu_3 = +\mu_4$) led to the same low residual factor. The refinements have been done starting with the arrangement $+\mu_1 = -\mu_2 = +\mu_3 = +\mu_4$ in the chemical cell and considering an inversion of the moment directions for each translation of the chemical cell along (1 0 0), (0 1 0) and (0 0 1), respectively. The refined values are the moment value μ_{Dy}, and the Euler angles θ_{Dy} and ϕ_{Dy}.

The results of the final refinements of the two H.T. and L.T. magnetic structures are summarized in Table 4 and the new L.T. antiferromagnetic structure is depicted in Fig. 8. The magnetic structure can be viewed as ferromagnetic (2 6 2) planes antiferromagnetically coupled along the stacking direction. The local arrangement of the moments (corresponding to the shortest distances in the Dy–Dy pairs) is depicted in Fig. 8b and the observed phase differences between the moments are summarized in Table 3. As for $TbSn_2$, the local arrangement is characterized by many frustrated situations: d_1 and $d_{1'}$ in the trigonal face of the prism, d_5 and $d_{5'}$ in the shortest diagonal of the prism, d_4 and $d_{4'}$ in the stretched tetrahedron. There are only three non-frustrated pairs:

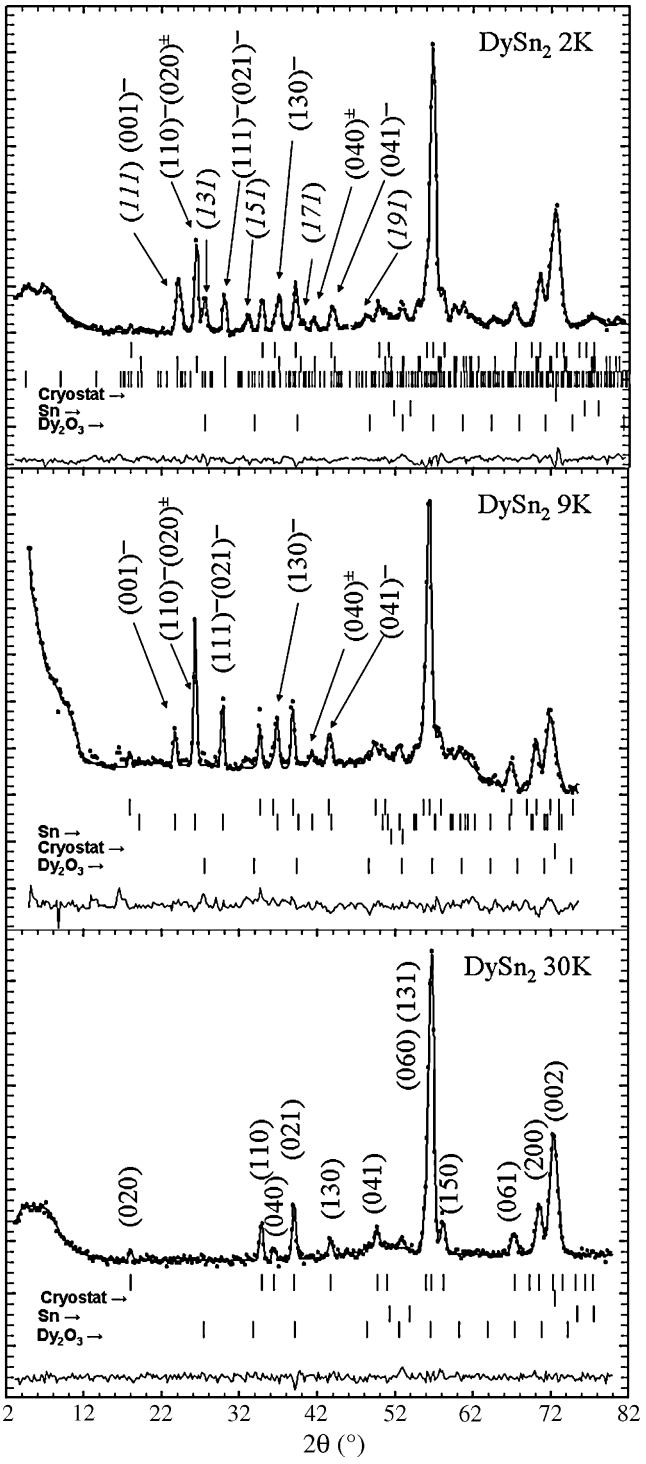

Fig. 7. Observed and calculated neutron diffraction patterns of $DySn_2$ at 30 and 2 K (indexation in italics refer to the antiferromagnetic structure).

d_3 (antiparallel arrangement along [1 0 0]), d_2 (antiparallel arrangement along [0 0 1]) and d_6 (parallel arrangement along the diagonal of the pseudo-square).

5.3. Magnetic structures of $HoSn_2$

The neutron thermogram (Fig. 3) is similar to that observed for $TbSn_2$. Below $T_N \approx 8$ K, it is observed a growth of magnetic lines whereas these magnetic lines begin to vanish and some other ones grow below ≈5 K. These magnetic transitions should be clearly

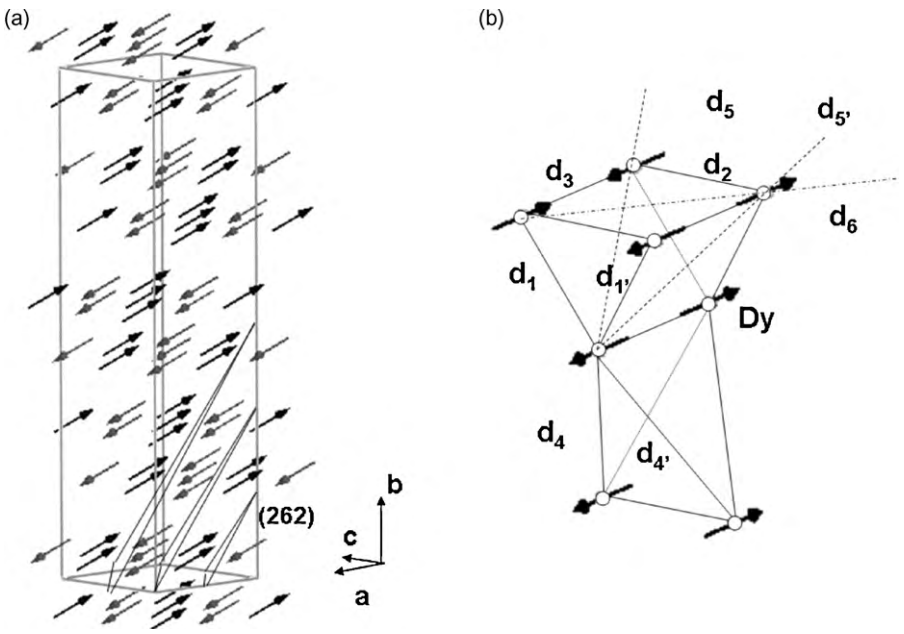

Fig. 8. Antiferromagnetic structure of $DySn_2$ (a) and local arrangement of the Dy moments in the trigonal prism and stretched tetrahedron (b).

related to those observed by magnetic measurements at 7.8 and 4.8 K (Fig. 2).

The pattern recorded at 5.6 K (Fig. 9) is similar to those previously observed for $TbSn_2$ and $DySn_2$ yielding a quite similar propagation vector $k = (0.3918(2), 0, 0.4197(2))$ and the same conclusions. The results of the refinements are given in Table 5.

In contrast, the low temperature pattern (Fig. 9c) is quite different to those observed of $TbSn_2$ and $DySn_2$. The magnetic Bragg angles are rather similar to those observed for the compounds HoT_xSn_2 (T = Fe, Co, Ni) previously studied [2,3,7]. The magnetic structure of these compounds is characterized by the propagation vector $k = (1/2, 1/2, 0)$ and the main feature in their diffraction patterns is the missing of the $(1/2, 5/2, 0)$ line. In Ref. [7], we have shown that the zero net value of the corresponding structure factor is only compatible with the moment arrangement $\mu_1 = \mu_3 = \mu_4 = -\mu_2$. The refinements have been undertaken considering this model. The results of the final refinements are gathered in Table 5. The antiferromagnetic structure is depicted in Fig. 10.

The local arrangement of the moments (corresponding to the shortest distances in the Ho–Ho pairs) is depicted in Fig. 10b and the observed phase differences between the moments are summarized in Table 3. With respect to the magnetic structure of $TbSn_2$, there are a less number of frustrated situations: only d_4 and $d_{4'}$ in the stretched tetrahedron. The trigonal face of the prism (d_1, $d_{1'}$ and

Table 4
Refined parameters of $DySn_2$ at 30, 9 and 1.9 K.

T	30 K	9 K	1.9 K
a (Å)	4.377(2)	4.376(9)	4.376(2)
b (Å)	16.158(8)	16.16 (1)	16.161(4)
c (Å)	4.283(2)	4.268(8)	4.268(1)
y_{Dy}	0.0989(7)	0.0989(9)	0.0998(6)
y_{Sn_1}	0.435(1)	0.442(2)	0.434(1)
y_{Sn_2}	0.749(1)	0.754(2)	0.751(1)
f_{corr}	0.05(2)	0.15(1)	0.09(1)
$A_{Dy}(I)$ (μ_B)	0	9.87(1)	9.1(1)
θ_{Dy} (°)	–	9(5)	24(3)
ϕ_{Dy} (°)	–	90	90
α_{Dy} (°)	–	227(6)	272(6)
q_x	–	0.3921(5)	0.3924(4)
q_y	–	0	0
q_z	–	0.4150(4)	0.4138(3)
$\mu_{Dy}(III)$ (μ_B)	0	–	4.2(1)
θ_{Dy} (°)	–	–	27(4)
ϕ_{Dy} (°)	–	–	90
q_x	–	–	1/2
q_y	–	–	1/2
q_z	–	–	1/2
r_{Bragg}; r_f	3.57; 4.52	8.58; 5.78	3.32; 2.94
$r_{magnI,II}$	–; –	12.7; –	10.7; 8.22
R_{wp}; R_{exp}	10.9; 9.05	16.6; 7.60	10.3; 4.57
χ^2	1.73	4.78	5.06

Table 5
Refined parameters of $HoSn_2$ at 20, 5.6 and 1.9 K.

T	20 K	5.6 K	1.9 K
a (Å)	4.359(2)	4.358(1)	4.358(1)
b (Å)	16.111(9)	16.103(4)	16.083 (3)
c (Å)	4.276(2)	4.274(1)	4.269(1)
y_{Ho}	0.099(1)	0.0993(4)	0.0979(4)
y_{Sn_1}	0.440(1)	0.4387(8)	0.441(1)
y_{Sn_2}	0.747(1)	0.7455(7)	0.749(1)
f_{cor}	0.07(1)	0.08(1)	0.07(1)
$A_{Ho}(I)$ (μ_B)	0	4.27(2)	0
θ_{Ho} (°)	–	20(1)	–
ϕ_{Ho} (°)	–	90	–
α_{Ho} (°)	–	248(4)	–
q_x	–	0.3918(2)	–
q_y	–	0	–
q_z	–	0.4197(2)	–
$\mu_{Ho}(II)$ (μ_B)	0	0	7.4(8)
θ_{Ho} (°)	–	–	0
ϕ_{Ho} (°)	–	–	90
q_x	–	–	1/2
q_y	–	–	1/2
q_z	–	–	0
r_{Bragg}; r_f	4.28; 7.16	2.90; 4.07	5.97; 7.70
$r_{magnI,II}$	–; –	7.23; –	–; 3.38
R_{wp}; R_{exp}	8.46; 2.38	8.56; 3.38	9.99; 1.46
χ^2	16.6	7.99	47.0

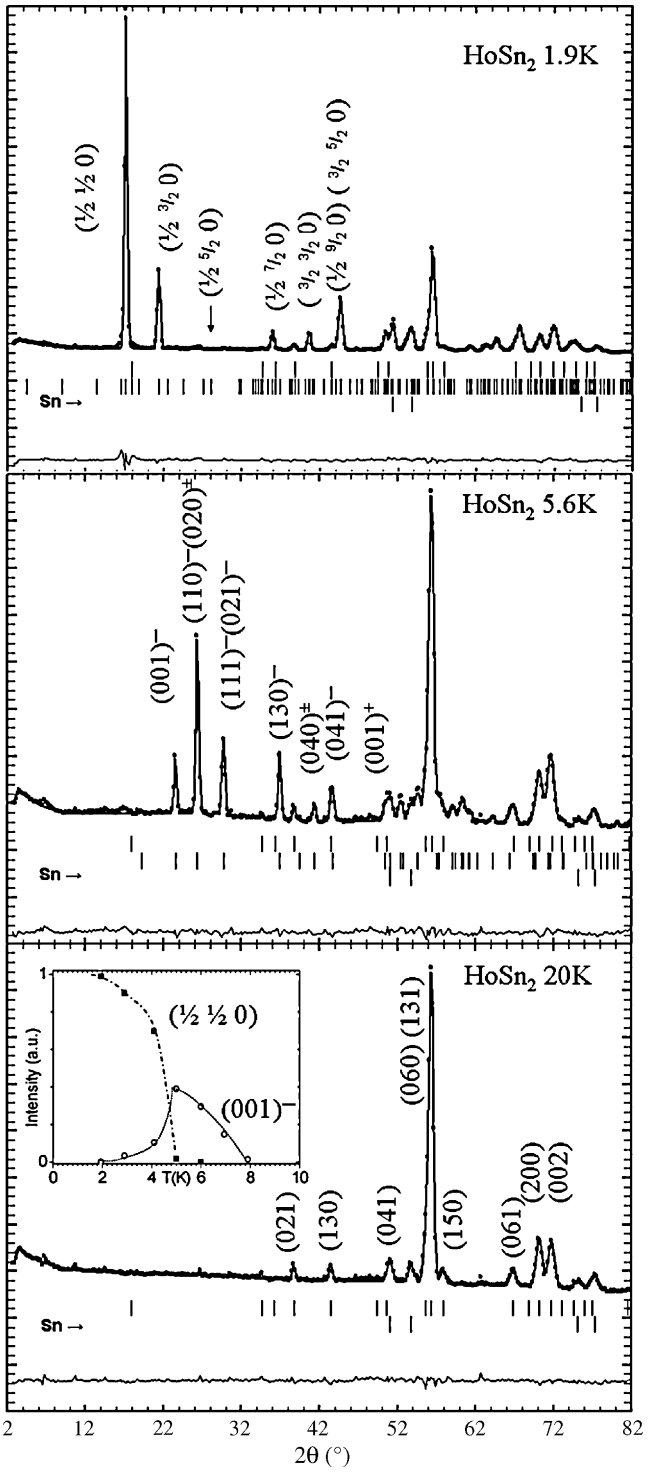

Fig. 9. Observed and calculated neutron diffraction patterns of $HoSn_2$ at 20, 5.6 and 1.9 K (insert show the variation of several typical lines).

d_2) is now in a parallel arrangement, the height of the prism (d_3) and the diagonals (d_5, $d_{5'}$ and d_6) in an antiparallel arrangement.

5.4. Magnetic structures of $ErSn_2$

Below $T_N \approx 5$ K, one observes a growth of magnetic lines in fair agreement with the small peak observed on the thermomagnetic curve at 4.5 K (Fig. 2).

Table 6
Refined parameters of $ErSn_2$ at 4.8, 4.0 and 1.5 K.

T	4.8 K	4.0 K	1.5 K
a (Å)	4.351(3)	4.346(1)	4.345(1)
b (Å)	16.07(1)	16.038(3)	16.0365(3)
c (Å)	4.268(3)	4.265(1)	4.264(1)
y_{Er}	0.106(2)	0.1003(5)	0.0991(4)
y_{Sn_1}	0.434(2)	0.4343(8)	0.4356(9)
y_{Sn_2}	0.746(2)	0.7467(7)	0.7456(8)
f_{corr}	0.01(2)	0.01(1)	0.03(1)
$A_{Er}(I)$ (μ_B)	0	6.01(4)	8.69(5)
$A_{Er3k}(I')$ (μ_B)	0	0	1.78(6)
θ_{Er} (°)	–	90	90
ϕ_{Er} (°)	–	0	0
α_{Er} (°)	–	275(3)	280(2)
q_x	–	0.3853(2)	0.3895(2)
q_y	–	0	0
q_z	–	0.4225(1)	0.4219(1)
$\mu_{Er}(II)$ (μ_B)	0	0	2.07(8)
θ_{Er} (°)	–	–	90
ϕ_{Er} (°)	–	–	0
q_x	–	–	0
q_y	–	–	0
q_z	–	–	1/2
r_{Bragg}; r_f	5.47; 7.22	1.38; 2.73	1.99; 2.24
$r_{magnI,II,III}$	–; –; –	6.43; –; –	4.60; 14.8; 22.8
R_{wp}; R_{exp}	10.9; 8.35	6.73; 3.19	7.77; 2.19
χ^2	2.45	5.07	12.6

The pattern recorded at 4 K (Fig. 11) is similar to those previously observed for $TbSn_2$, $DySn_2$ and $HoSn_2$ yielding a quite similar propagation vector (0.3853(2), 0 0.4225(1)) and the same conclusions. The results of the refinements are gathered in Table 6. The main change observed with respect to the previous compounds is the orientation of the moments which is aligned along the [1 0 0] direction.

The patterns recorded below 2 K are mainly characterized by the growth of three additional lines at $\theta \approx 14°$, 19° and 33° (Fig. 11). Two of them ($\theta \approx 19°$ and 33°) are compatible with the AF1 structure observed for $TbSn_2$ and $DySn_2$, already reported for the compounds ErT_xSn_2 (T = Fe, Co, Ni) [5,7]. The last one at $\theta \approx 14°$ may be indexed as a third harmonic of the propagation vector related to the remaining high temperature magnetic structure. The refinements have been undertaken considering a mixture of the high temperature sine-modulated structure, its third harmonic and the AF1 structure. The results are given in Table 6 and the magnetic structure is depicted in Fig. 12. As for $TbSn_2$ and $DySn_2$ the local arrangement is characterized by many frustrated situations (see Sections 5.1 and 5.2).

5.5. Magnetic structures of $TmSn_2$

Below $T_N \approx 4.0$ K, one observes the growth of a set of magnetic lines which are quite different to those observed in the previous LSn_2 compounds (L = Tb–Er) (Fig. 13). The pattern recorded at 3.9 K displays some similarity with the pattern of $TmFe_{0.1}Sn_2$ characterized by a sine-modulated structure with propagation vector k = (0, 0.7196, 0.4381) [7]. However, in the present case, the propagation vector components are refined to significantly different values: $q_y = 0.665(2)$ and $q_z = 0.3768(3)$. According to the observed satellites, the refinements have been done considering a C-centred sine-modulated structure with as free variables: the maximum moment amplitude A_{Tm}, the phase angle α_{Tm} between the atoms related by the c-glide plane and the Euler angles θ_{Tm} and ϕ_{Tm}. The results are given in Table 7.

Below $T \approx 3$ K, we observe the growth of an additional line around $2\theta = 5°$ which can be indexed as a satellite arising from a third harmonic contribution.

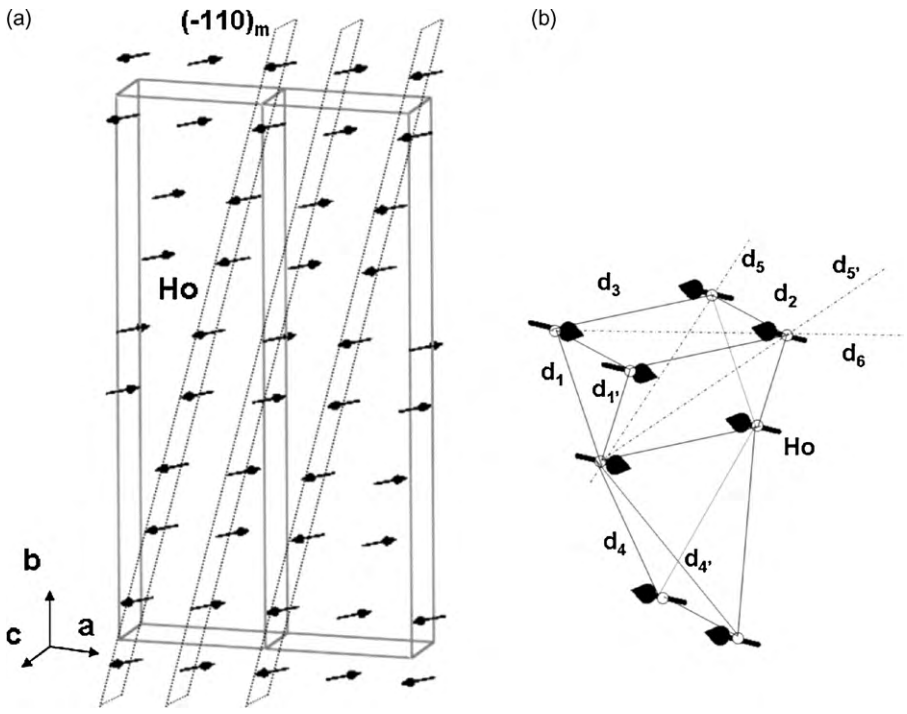

Fig. 10. Antiferromagnetic structure of $HoSn_2$ (a) and local arrangement of the Ho moments in the trigonal prism and stretched tetrahedron (b).

The magnetic structure and the local arrangement of the moments (corresponding to the shortest distances in the Tm–Tm pairs) are depicted in Fig. 14 and the observed phase differences between the moments are summarized in Table 3. There are some similarities with the AF structure of Tb, namely the phase differences corresponding d_2 and d_6 are close to 180° and that of d_3 is 0°. The phase differences corresponding to the frustrated situations in the terbium compound seem to indicate an antiparallel character for d_1 and d_5.

6. Discussion

The neutron diffraction study of the LSn_2 series (L = Tb–Tm) shows that the L sublattice orders, in a first step, in a sine-modulated structure in all the compounds. The ordering temperature T_N decreases continuously from terbium to thulium and rather well follows the evolution of the de Gennes factor (Fig. 15) except for $TmSn_2$, which displays a particular sine-modulated structure.

Except for $TmSn_2$, we observe, at lower temperature, a second transition from the sine-modulated structure towards a simple commensurate antiferromagnetic state. The transformation is complete in $TbSn_2$ and $HoSn_2$ while, in the case of $DySn_2$ and $ErSn_2$, we observed, even at the lowest temperature investigated (1.5 K), the coexistence of the high temperature sine-modulated structure and the low temperature commensurate antiferromagnetic order.

The antiferromagnetic order observed for $TbSn_2$ and $ErSn_2$ is equivalent to that observed in the LT_xSn_2 (L = Tb, Er, T = Fe, Co, Ni) compounds and will be labelled AF1. The antiferromagnetic order observed for $HoSn_2$ is equivalent to that observed in the HoT_xSn_2 (T = Fe, Co, Ni) series and will be labelled AF2. The antiferromagnetic order detected in $DySn_2$ is of a new type characterized by the doubling of the three parameters of the chemical cell and will be labelled AF3. The sine-modulated structure observed for LSn_2 (L = Tb–Er), already reported for $DyNi_{0.22}Sn_2$ [4], will be labelled SM1 and the one observed for $TmSn_2$, already reported for $TmFe_{0.1}Sn_2$ [7], will be labelled SM2.

Table 8 summarizes the occurrence of these five magnetic structure-types in the LT_xSn_2 and LSn_2 (L = Tb–Tm; T = Fe, Co, Ni) families. It is worth noting (i) the predominance of the AF1 magnetic structure (ii) the similar behaviour of the Tb and Er compounds (iii)

Table 7
Refined parameters of $TmSn_2$ at 6, 3.9 and 1.45 K.

T	6 K	3.9 K	1.45 K
a (Å)	4.350(2)	4.348(1)	4.348(1)
b (Å)	15.98(2)	15.961(4)	15.946(3)
c (Å)	4.254(2)	4.260(1)	4.258 (1)
y_{Tm}	0.101(1)	0.098(1)	0.0980(5)
y_{Sn_1}	0.434(1)	0.437(1)	0.435(1)
y_{Sn_2}	0.748(1)	0.746(1)	0.7465(9)
f_{corr}	0.13(1)	0.04(1)	0.11(1)
A_{Tm} (μ_B)	–	4.77(6)	8.30(5)
A_{Tm3k} (μ_B)		0	1.34(3)
θ_{Tm} (°)	–	90	90
ϕ_{Tm} (°)	–	0	0
α_{Tm} (°)	–	−127(3)	−128(1)
q_x	–	0	0
q_y	–	0.665(2)	0.6671(5)
q_z	–	0.3768(3)	0.3803(1)
r_{Bragg}; r_f	1.91; 4.33	2.66; 3.07	3.15; 2.65
r_{magn}; r_{magn3}	–; –	13.6; –	5.42; 8.12
R_{wp}; R_{exp}	6.54; 4.16	3.54; 2.41	7.87; 1.06
χ^2	4.72	2.31	55.0

Table 8
Stable magnetic structures of LSn_2 and LT_xSn_2 compounds.

	LSn_2	LFe_xSn_2	LCo_xSn_2	LNi_xSn_2
Tb	AF1 ↔ SM1	AF1 [7]	AF1 [3]	AF1 [2]
Dy	AF3 ↔ SM1	AF1 [7]	–	SM1 [4]
Ho	AF2 ↔ SM1	AF2 [7]	AF2 [3]	AF2 [2]
Er	AF1 ↔ SM1	AF1 [7]	AF1 [5]	AF1 [5]
Tm	SM2	AF1 ↔ SM2 [7]	–	–

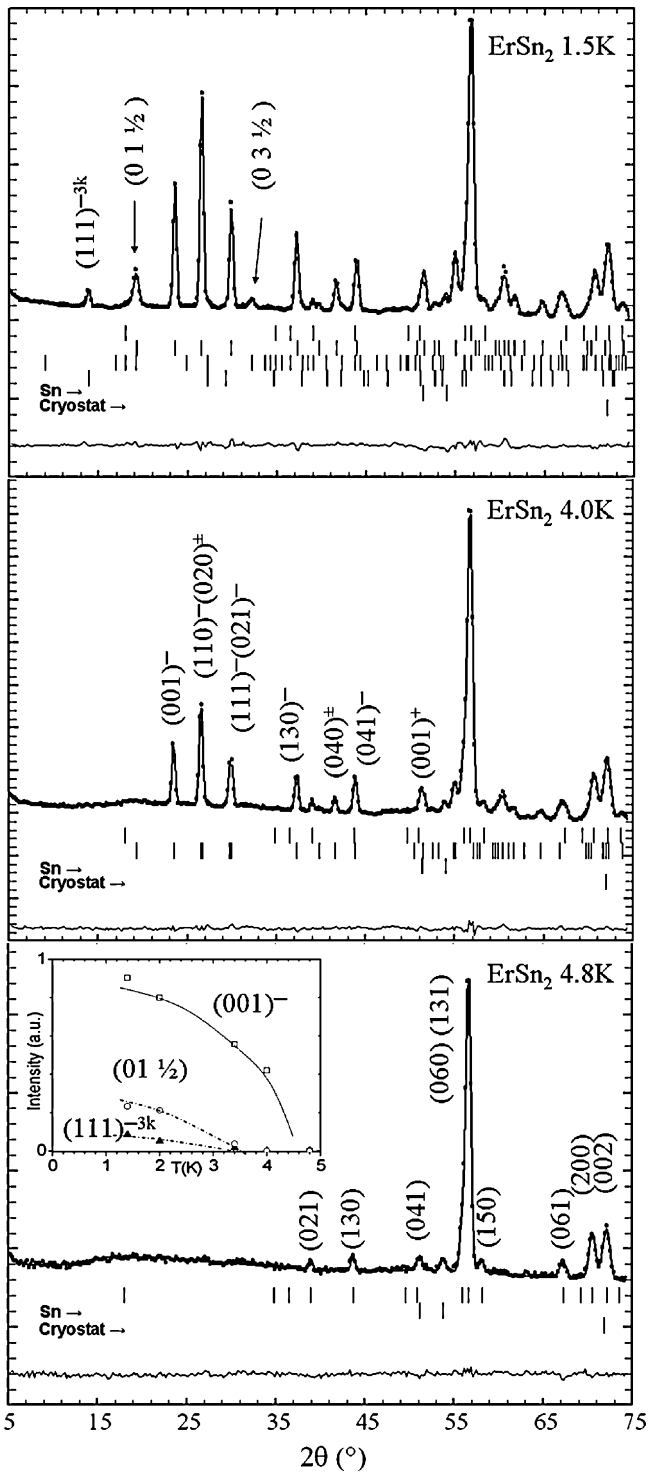

Fig. 11. Observed and calculated neutron diffraction patterns of $ErSn_2$ at 4.8, 4.0 and 1.5 K (insert shows the variation of several typical lines).

the particular stability of the AF2 structure for the holmium representatives (iv) the SM2 structure for the actually studied thulium compounds and, finally, the more complicated behaviour of the dysprosium compounds.

Besides this large variety of magnetic orderings, it worth noting that we observe, for LSn_2 compounds, temperature induced transitions between the same SM1 structure and the different AF1, AF2 and AF3 orderings. Neglecting the observed differences between the refined magnetic parameters of the SM1 structure, it may be

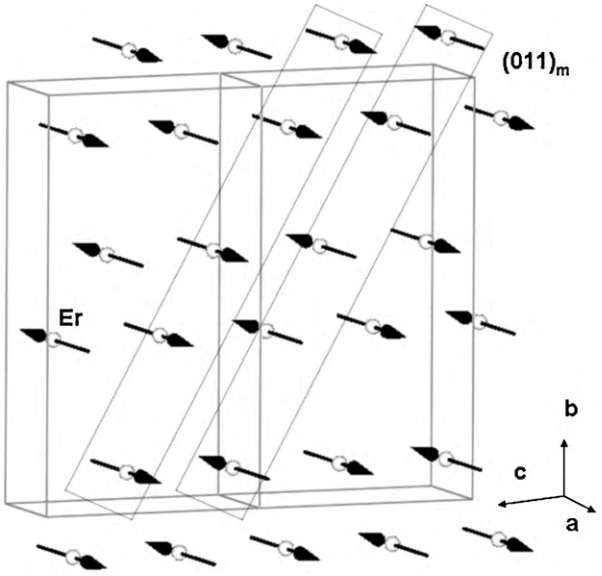

Fig. 12. Antiferromagnetic structure of $ErSn_2$.

assumed that the three antiferromagnetic structures, which are in equilibrium with the common SM1 incommensurate structure, should have close energies of stabilisation.

On another hand, the three antiferromagnetic AF1, AF2 and AF3 structures display several interesting characteristics. The L sublattice is constituted of pseudo-square planes perpendicular to the [0 1 0] direction. In a magnetic point of view, we observe different arrangements in this plane:

(i) antiparallel arrangement along [1 0 0] in the AF2 structure ($k = (1/2, 1/2, 0)$),
(ii) antiparallel arrangement along [0 0 1] in the AF1 structure ($k = (0, 0, 1/2)$),
(iii) antiparallel arrangement along [1 0 0] and [0 0 1] in the AF3 structure ($k = (1/2, 1/2, 1/2)$).

Owing to the presence of the *c*-glide and *n*-glide planes in the $ZrSi_2$ structure, these different in-plane arrangements allow (*or not*) the play of specific interlayer interactions as depicted in Fig. 16 and summarized in Table 9.

Considering the successive interlayer interactions $J_{0.2}$, $J_{0.3}$, ... related to the interlayer spacings $d_{L-L} = 0.2b$, $0.3b$, ... (*according to* $y_L \approx 0.1$), we note that there are different frustrations of the interlayer interactions depending on the in-plane ordering. The antiparallel arrangement along [1 0 0] leads to frustrated interactions for the interlayer spacing $d_{L-L} = 0.3b$, $0.5b$ and $0.7b$. The antiparallel arrangement along [0 0 1] leads to frustrated interactions for the interlayer spacings $d_{L-L} = 0.2b$, $0.3b$, $0.7b$ and $0.8b$. For the AF3 structure, the antiparallel arrangement along both the [0 0 1] and [1 0 0] directions combine these two conditions with frustrated interactions for the spacings $d_{L-L} = 0.2b$, $0.3b$, $0.5b$, $0.7b$ and $0.8b$ and the first non-zero interlayer interaction corresponds to the lattice translation $d_{L-L} = 1.0b$. It is interesting to note that none of the actual in-plane configurations enables the expression of the $J_{0.3}$ and $J_{0.7}$ interactions which can play a role only with a parallel in-plane arrangement, a case never observed in these $ZrSi_2$-type stannides.

If we now consider that the strength of the interlayer interactions decreases with the increase of the interlayer spacing and if we assume, as discussed above, that the three AF structures should have close energies of stabilisation, we guess that:

Table 9
Frustration of the interlayer interactions as a function of the propagation vector (see also Fig. 16).

k	$J_{0.2}$	$J_{0.3}$	$J_{0.5}$	$J_{0.7}$	$J_{0.8}$	$J_{1.0}$
[0, 0, 0]	–	–	–	–	–	–
[1/2, 1/2, 0]	–	Frustrated	Frustrated	Frustrated	–	–
[0, 0, 1/2]	Frustrated	Frustrated	–	Frustrated	Frustrated	–
[1/2, 1/2, 1/2]	Frustrated	Frustrated	Frustrated	Frustrated	Frustrated	–

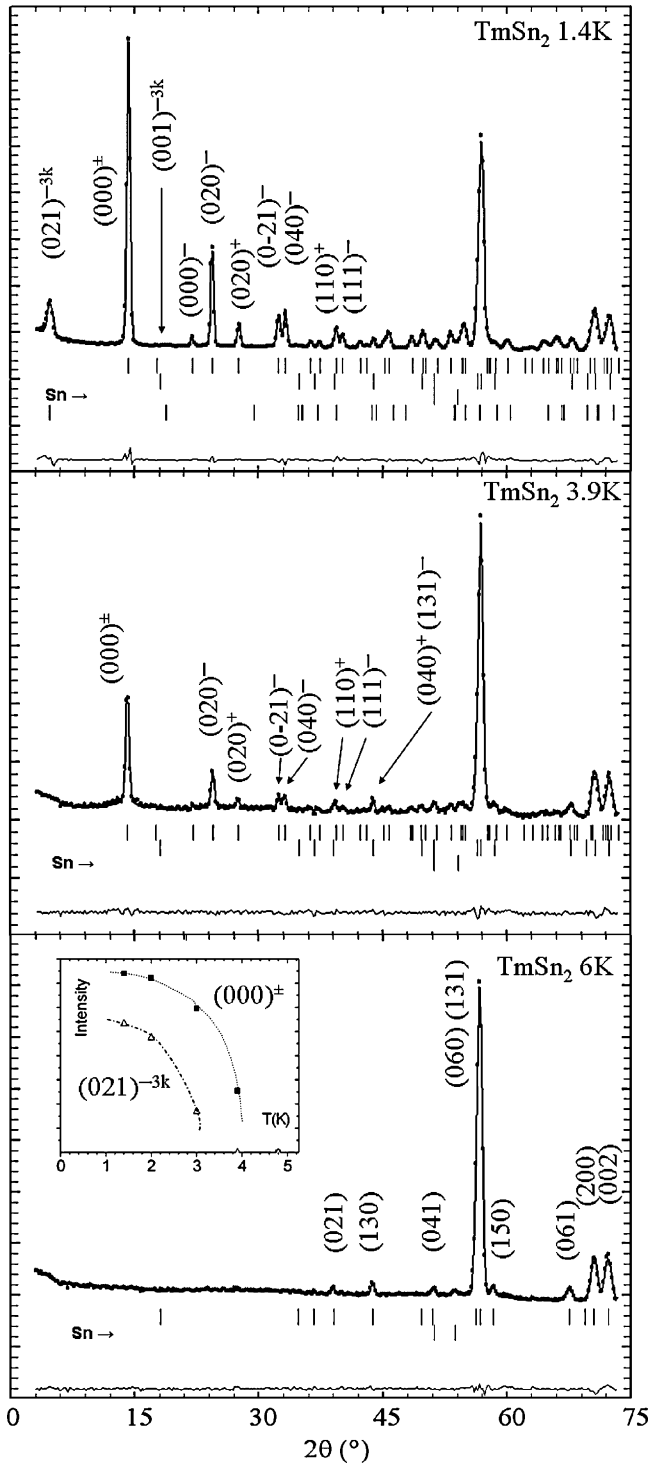

Fig. 13. Observed and calculated neutron diffraction patterns of $TmSn_2$ at 6, 3.9 and 1.45 K (insert shows the variation of several typical lines).

- the AF1 structure is stabilised by both medium interlayer and in-plane interactions;
- the AF2 structure is stabilised by strong interlayer interaction and weak in-plane interactions;
- the AF3 structure is stabilised by weak interlayer interactions and strong in-plane interactions.

These conclusions suggest that the stabilisation of each structure will result from a subtle balance between the variations of both the in-plane and interlayer interactions.

Remark: The occurrence of the AF3 magnetic structure is rather surprising since it looks like there were almost no interlayer interactions. Inversely, we guess that the stability of this structure should arise from a particularly stable in-plane configuration.

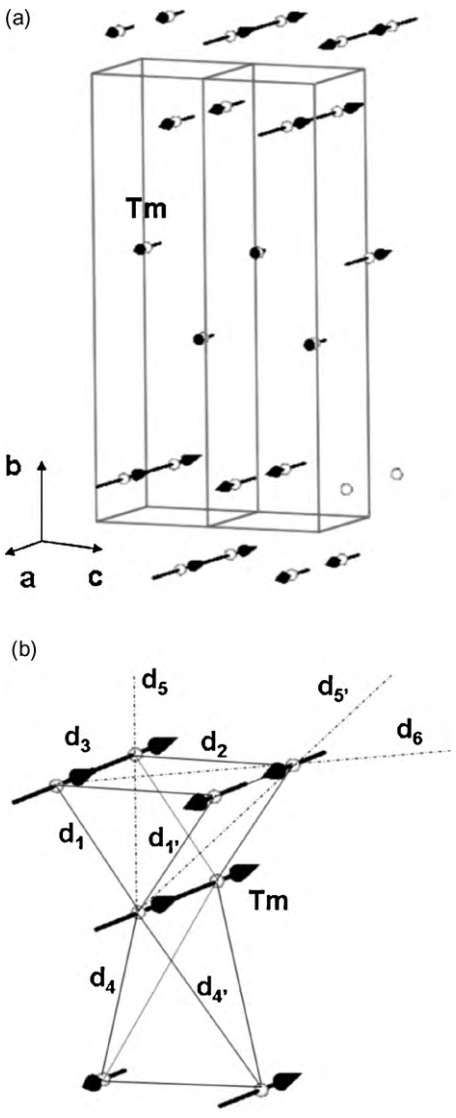

Fig. 14. Sine-modulated magnetic structure of $TmSn_2$ at 1.45 K (a) and local arrangement of the Tm moments in the trigonal prism and stretched tetrahedron (b).

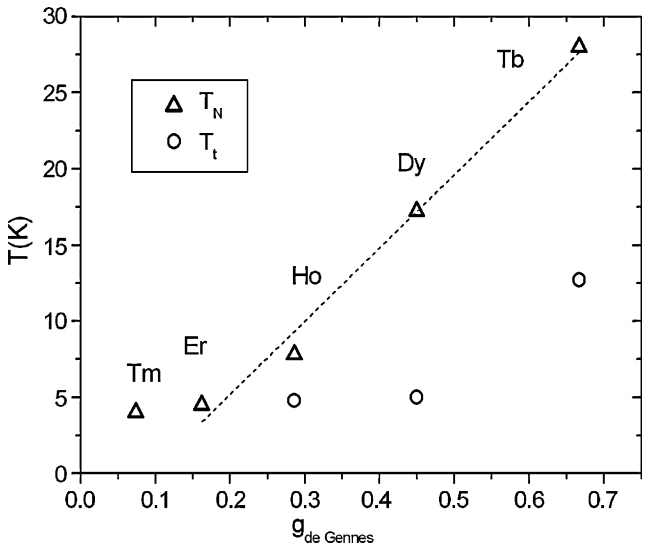

Fig. 15. Variation of the transition temperatures as a function of the de Gennes factor.

The observed 3D-orderings provide other information.

In the case of the AF3 structure, for which the first non-zero interlayer interaction is $J_{1.0}$, the propagation vector $k=(1/2, 1/2, 1/2)$ indicates that the lattice translation along [0 1 0] is associated to an antiparallel arrangement. A similar behaviour is observed for the AF2 structure ($k=(1/2, 1/2, 0)$) also characterized by the doubling of the b axis.

As shown in Table 9, the AF1 structure ($k=(0, 0, 1/2)$) takes into account the $J_{0.5}$ interaction and we note that there is no doubling of the b axis. This feature should be also related to frustration effects. Thus, in the case of a doubling of the b axis, the $J_{0.5}$ interaction would be also frustrated. The occurrence of the AF1 structure indicates that, logically, the $J_{0.5}$ interaction dominates the $J_{1.0}$ interaction. The moment arrangement in the AF1 structure is characterized by the anti-C translation mode.

Finally, the AF2 structure takes into account the $J_{0.2}$ and $J_{0.8}$ interlayer interactions. The $J_{0.2}$ interaction is mainly characterized by the moments ordering in the L_6 trigonal prisms, involving specifically the two shortest diagonals (d_5 and $d_{5'}$) and the shortest L–L contact ($d_1 \approx 3.8$ Å). The description of the AF2 structure shows that the triangular face of the prism displays a parallel arrangement and that the L moments linked by the shortest diagonals are characterized by an antiparallel arrangement. It is worth noting that the alternative arrangement in a hypothetical AF2′ structure is not observed (Fig. 17). This order corresponds to the moment arrange-

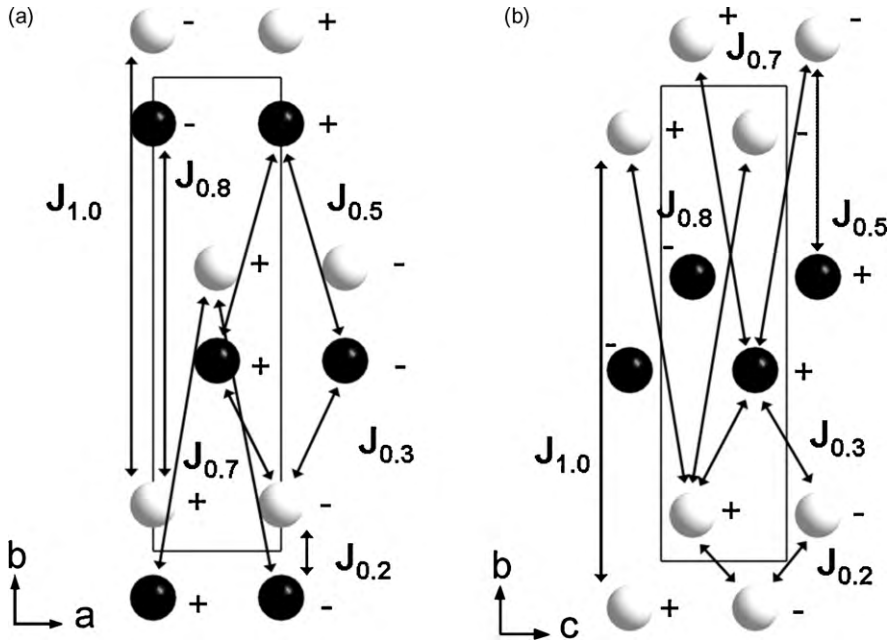

Fig. 16. Relative interlayer arrangements in the antiferromagnetic structures of $HoSn_2$ (a) and $TbSn_2$ (b). J_i are the exchange interactions between (0 1 0) planes related to the interlayer spacings $d_{L-L} = 0.2b, 0.3b, \ldots$ (*according to* $y_L \approx 0.1$).

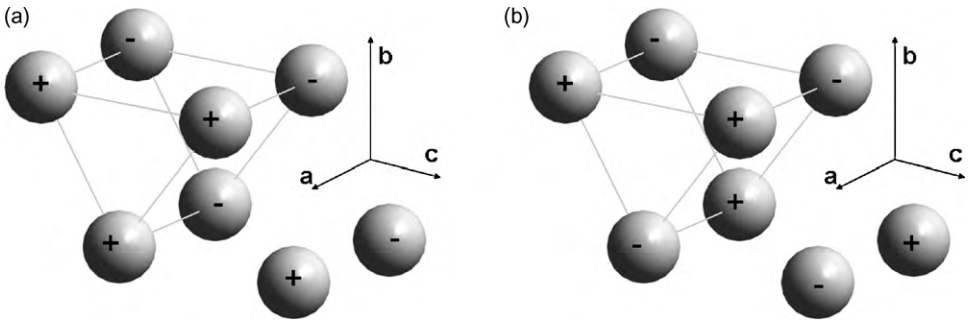

Fig. 17. Moment arrangement in the trigonal prism in $HoSn_2$ (a) an the alternative arrangement in a hypothetical AF2′ structure (b).

ment $\mu_1 = \mu_2 = \mu_4 = -\mu_3$ which will maximize the structure factor of the (1/2, 5/2, 0) line. The observed AF2 structure suggests that the interactions in the triangular face of the prism are ferromagnetic and/or that the interactions along the shortest diagonals are antiferromagnetic.

Regarding the magnetocrystalline anisotropy of the L moment, it is worthwhile to note that the moment directions observed in the LSn_2 compounds are similar to those observed in corresponding LFe_xSn_2 and closely related to the sign of the α_j Steven's coefficients. The moment of the atoms L characterized by a negative α_j coefficient (Tb, Dy, Ho) lies along the [0 0 1] direction or close to this direction. The moment of the atoms L characterized by a positive α_j coefficient (Er, Tm) lies along the [1 0 0] direction.

7. Conclusion

The magnetic properties of the $ZrSi_2$-type LSn_2 stannides display a very interesting panel of magnetic behaviours. The compounds $TbSn_2$, $DySn_2$, $HoSn_2$ and $ErSn_2$ are characterized by three different collinear antiferromagnetic structures at low temperature and by a similar incommensurate sine-modulated structure at higher temperature. This property roughly enables us to draw a relative stability scale of the different magnetic arrangements within the (a, c) plane. A careful analysis of the magnetic structures shows that, due to the crystallographic characteristics of the $ZrSi_2$ structure, the in-plane and interplane interactions are strongly inter-dependent, a feature which can explain the rather complicated magnetic behaviour observed in this family. It might be now interesting to complete the isotypic LT_xSn_2 series (see Table 8) in order to collect information on the factors governing the stability of each moment configuration.

Acknowledgements

We are indebted to the Institute Laue Langevin (Grenoble, France) for the provision of research facilities.

References

[1] M. Francois, G. Venturini, B. Malaman, B. Roques, J. Less Common Met. 160 (1990) 197.
[2] A. Gil, B. Penc, S. Baran, J. Hernandez-Velasco, A. Szytula, A. Zygmunt, J. Alloys Compd. 361 (1–2) (2003) 32.
[3] A. Gil, B. Penc, E. Wawrzynska, J. Hernandez-Velasco, A. Szytula, A. Zygmunt, J. Alloys Compd. 365 (1–2) (2004) 31.
[4] A. Gil, B. Penc, J. Hernandez-Velasco, A. Szytula, A. Zygmunt, Physica B: Condens. Matter 350 (1–3) (2004) E119.
[5] B. Penc, E. Wawrzynska, A. Szytula, A. Gil, J. Hernandez-Velasco, A. Zygmunt, J. Alloys Compd. 375 (1–2) (2004) L1.
[6] L.C.J. Pereira, D.P. Rojas, J.C. Waerenborgh, Intermetallics 13 (1) (2005) 61.
[7] B. Malaman, G. Venturini, J. Alloys Compd., doi:10.1016/j.jallcom.2010.01.060.
[8] A. Palenzona, P. Manfrinetti, J. Alloys Compd. 201 (1993) 43.
[9] J. Rodriguez-Carvajal, Physica B 192 (1993) 55.
[10] P.G. Cotter, J.A. Kohn, R.A. Potter, J. Am. Ceram. Soc. 39 (1956) 11.
[11] A. Iandelli, A. Palenzona, Atti. Accad. Nazl. Lincei, Rend. Cl. Sci. Fis. Mat. Nat. 40 (1966) 623.
[12] V.N. Eremenko, M.V. Bulanova, P.S. Martensyuk, Sov. Prog. Chem. 57 (1990) 3.
[13] V.N. Eremenko, M.V. Bulanova, P.S. Martensyuk, J. Alloys Compd. 189 (1992) 229.
[14] G. Venturini, A. Mesbah, J. Alloys Compd. 458 (2008) 22.
[15] G. Venturini (private communication 2009).